

ISIS spallation neutron targets – confirmation of Monte Carlo activity calculations by measurement

D Findlay, G Škoro, G Burns

May 2020



©2020 UK Research and Innovation



This work is licensed under a [Creative Commons Attribution 4.0 International License](https://creativecommons.org/licenses/by/4.0/).

Enquiries concerning this report should be addressed to:

RAL Library
STFC Rutherford Appleton Laboratory
Harwell Oxford
Didcot
OX11 0QX

Tel: +44(0)1235 445384
Fax: +44(0)1235 446677
email: libraryral@stfc.ac.uk

Science and Technology Facilities Council reports are available online at:
<https://epubs.stfc.ac.uk>

ISSN 1358-6254

Neither the Council nor the Laboratory accept any responsibility for loss or damage arising from the use of information contained in any of their reports or in any communication about their tests or investigations.

ISIS spallation neutron targets — confirmation of Monte Carlo activity calculations by measurement

D J S Findlay, G P Škoro, G J Burns
Rutherford Appleton Laboratory, Oxon. OX11 0QH, UK

Abstract

Comparisons between measurements and calculations of activities of radionuclides in spent tantalum-clad tungsten targets from the ISIS Spallation Neutron Source are presented. Uncertainties in the measurements and the calculations are discussed. The overall conclusion is that radionuclide inventories calculated using the Monte Carlo codes MCNPX 2.70, HTAPE3X and CINDER-90 agree well with measurements.

1. Introduction

It is of fundamental interest and also of operational relevance to compare calculations of radioactivity in particle-accelerator-driven spallation neutron targets with actual measurements. With regard to the radioactivity induced in the 800-MeV-proton-driven tantalum-clad tungsten targets at the ISIS Spallation Neutron Source [1] at the Rutherford Appleton Laboratory, there are several good reasons to compare measurement and calculation, *viz*

- to provide confidence that when spent targets are disposed of as radioactive waste declared radionuclide inventories are sufficiently accurate;
- to provide confidence in estimates of thermal power dissipation within a target after beam switch-off ('decay heat'); and
- to provide confidence that complicated Monte Carlo computational procedures can in general be relied upon — especially as such complicated Monte Carlo computations can underpin multi-million-pound projects such as the ISIS TS-1 Project [2], a project for improving and extending the life of the ISIS First Target Station.

However, it is important to bear in mind that while measurements of activities of all radionuclides in spent spallation targets may be possible in principle, such measurements are not possible in practice because of the great difficulty and expense of the radiochemical work that would necessarily be involved. Inventories for spallation targets resulting from Monte Carlo calculations typically run to lists of activities of several hundred radionuclides, and many of these radionuclides do not provide measurable gamma-ray signatures; consequently many of the radionuclides would have to be chemically separated before their activities could be measured, which would imply complete chemical dissolution of the highly radioactive target in a specialised radiochemical facility. But even for the radionuclides that do have good gamma-ray signatures there are problems in practice; the measurement of the activity of a particular radionuclide may have to be carefully timed, since for too short cooling times after irradiation dose rates and gamma-ray backgrounds may be too high, whereas for too long cooling times the gamma-ray lines may have decayed into invisibility.

There are uncertainties in the particle-tracking procedures used in Monte Carlo computer codes such as MCNPX [3], for example from uncertainties in the physical and geometrical modelling, from uncertainties in cross-section values in the nuclear data libraries used, and, last but not least, from the consequences of choosing particular physics models for use in the MCNPX simulations. Estimated systematic uncertainties here can be at least $\pm 20\%$.

Consequently, comparisons between measurements and calculations cannot be expected to be made at the few per cent level; in practice, agreement between measurement and calculation to anywhere within $\sim 30\%$ must be accepted as being 'good'.

2. ISIS targets

The neutron-producing targets at the hearts of the two ISIS target stations are of two quite distinct designs. When ISIS began operations in 1984 the targets in the original target station (now called the First Target Station (TS-1)) were 23-plate depleted uranium targets; in the early 1990s a change was made to 12-plate tantalum targets; and finally, from 2001, in order to increase neutron output slightly, to reduce decay heat significantly, and to take advantage of the much better thermal conductivity of tungsten, 12-plate tantalum-clad tungsten targets have been used. Currently, TS-1 targets are driven by an 800-MeV proton beam delivering 200 μA at 40 pps (pulses per second). A schematic diagram of a TS-1 target is shown in Fig. 1.

The ISIS Second Target Station (TS-2) which began operations in 2008 was designed specifically for cold neutron work at 10 pps, and in order to maximise the number of neutrons in each pulse the whole target-reflector-and-moderators (TRAM) assembly was made more compact than the TS-1 TRAM assembly. TS-2 targets are driven by an 800-MeV proton beam delivering 40 μA at 10 pps, and since the TS-2 beam power is much less than the TS-1 beam power it was possible to make a TS-2 target as essentially a solid tungsten cylinder cooled only at the front end and on the curved surface. A schematic diagram of a TS-2 target is shown in Fig. 2.

3. Activity measurements on ISIS targets

Four sets of gamma-ray spectrometry measurements on activated ISIS targets have been made, two on tungsten targets W#2 and W#3 from the First Target Station (TS-1), and two on targets W#1, W#2 and W#3 and on W#6, W#7 and W#8 from the Second Target Station (TS-2). Details are given in Table 1, and a typical counting set-up is shown in Fig. 3.

Since it is impossible to make measurements with an HPGe gamma-ray detector on a 'bare' target (as an example, at the time of measurement, the dose rate 1 metre from the TS-1 W#3 target was $\sim 0.5 \text{ Sv hour}^{-1}$), gamma-ray spectrometry measurements were made through the $\sim 17\text{-cm}$ -thick lead (Pb) walls of transport or storage flasks. Such thick lead shielding inevitably skews the gamma-ray spectrum; gamma-rays below $\sim 1000 \text{ keV}$ become invisible because, in the energy region of relevance, the gamma-ray mass attenuation coefficient becomes larger as the gamma-ray energy decreases. A typical gamma-ray spectrum is shown in Fig. 4.

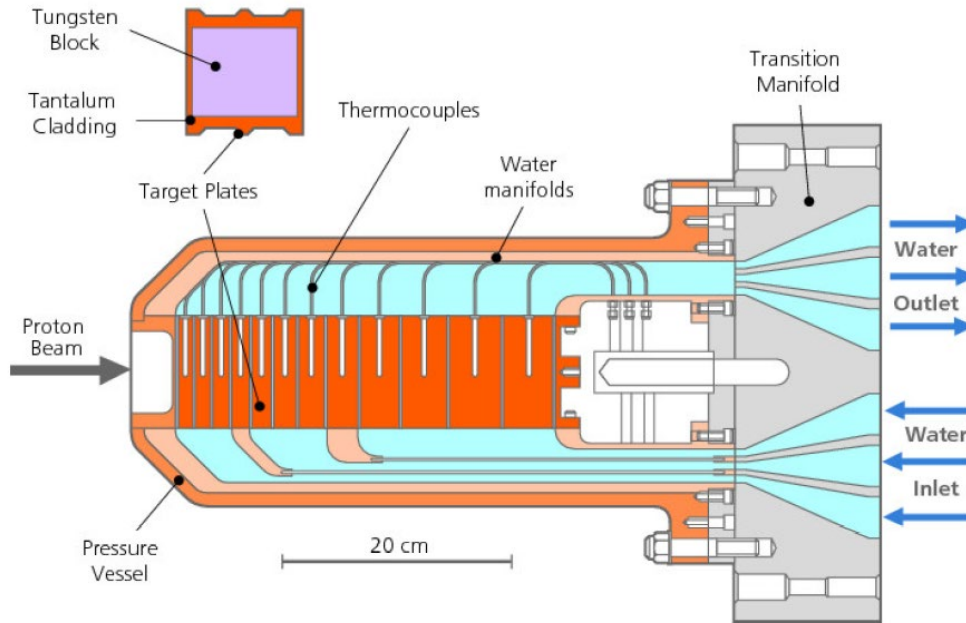


Fig. 1. Schematic drawing of an ISIS TS-1 target. Along the direction of the incident beam the thicknesses of tungsten in the target plates are 11.0, 11.0, 12.0, 13.5, 15.0, 18.0, 21.0, 26.0, 34.0, 40.0, 46.0 and 46.0 mm; each plate has 2.0 mm of tantalum cladding on each side; and each plate is separated from its neighbours by 2.0 mm of water. The pressure vessel fits closely over the structures containing and separating the channels through which the cooling water flows. The heavy water (D_2O) flow rate through the each of the three main channels is ~ 160 litres $minute^{-1}$, corresponding to a flow speed between the plates of ~ 5 $m\ s^{-1}$.

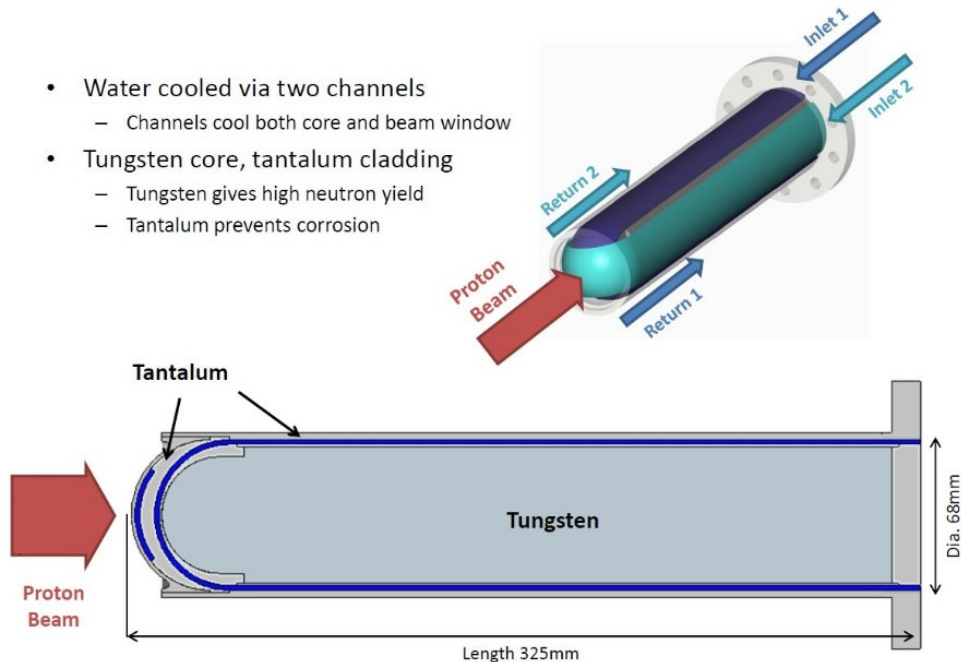


Fig. 2. Schematic drawing of an ISIS TS-2 target. Tantalum cladding thickness over tungsten core, 2.3 mm; thickness of tantalum outer casing, 2.3 mm; thickness of water channel between cladding and casing, 1.5 mm. Along axis from front of target: 1.5 mm Ta, 2.0 mm water, 6.0 mm Ta, 2.0 mm water, 3.5 mm Ta. Water (H_2O) circulates through each flow-and-return circuit at a rate of ~ 45 litres per minute, corresponding to a flow speed of ~ 10 $m\ s^{-1}$.

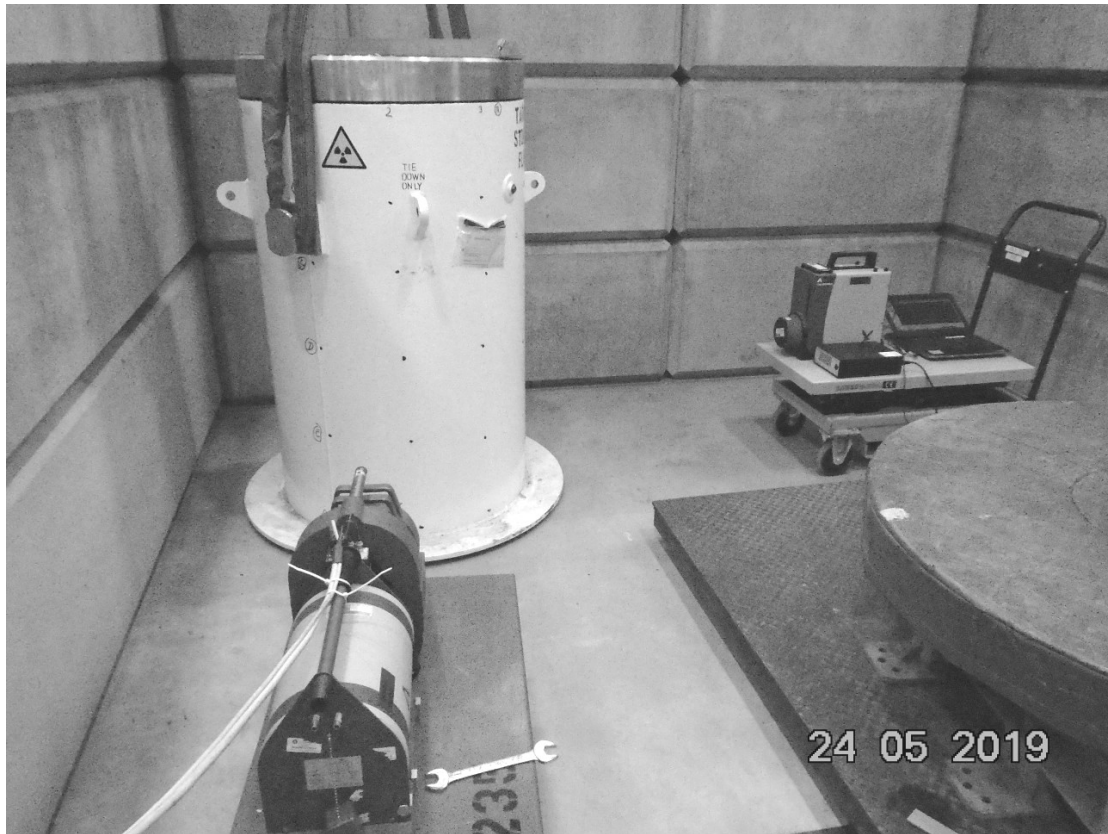


Fig. 3. Typical gamma-ray counting set-up in a concrete-block-shielded area in Building R105 at RAL. A Canberra BE3825 HPGe gamma-ray detector can be seen towards the lower left-hand corner of the photo, and a Canberra BE2830 can be seen towards the right-hand side of the photo. The storage flask containing the target(s) being measured has the following dimensions: cavity diameter 552 mm; cavity steel wall thickness 6 mm; lead thickness 170 mm; flask outer steel wall thickness 15 mm; flask outer diameter 934 mm.

Target(s)	Irradiated	Integrated beam current delivered, mA-hours	Cooling time ¹ before γ spec. meas., years
TS-1 W#2	Sep. 2005 – Mar. 2009	1946	7.63
TS-1 W#3	May 2009 – Aug. 2014	2903	4.76
TS-2 W#1	Sep. 2008 – Dec. 2009	115	4.78
W#2	Feb. 2010 – May 2010	36	
W#3	Mar. 2011 – Nov. 2012	212	
TS-2 W#6	Jul. 2014 – Jul. 2015	103	0.72
W#7	Sep. 2015 – Jun. 2017	280	
W#8	Sep. 2017 – Mar. 2019	232	

Table 1. Irradiation parameters for ISIS targets measured by gamma-ray spectrometry. For each target the integrated proton beam charge was delivered in a series of irradiation campaigns ('user cycles') each ~30–50 days long.

¹ For TS-2 targets, cooling times measured from the last-irradiated targets (W#3 and W#8).

There are three key components involved in the process of extracting the absolute activity A of a radionuclide from a gamma-ray spectrum: the gamma-ray source term, absorption of gamma-rays between the gamma-ray source and the gamma-ray detector, and the absolute counting detection efficiency of the detector. In essence, the count rate C_i in a gamma-ray detector is $C_i = \alpha_i \eta_i \varepsilon_i A$ where α_i is the probability of emission (or ‘abundance’) of gamma-ray i when the nucleus decays, η_i is the attenuation factor due to absorption, and ε_i is the full-energy-peak detection efficiency of the gamma-ray detector.

In some circumstances a gamma-ray source may be an ‘ideal’ point source, but more often the source is of finite dimensions (for example, since tantalum is distributed throughout the active volume of TS-1 targets (the dimensions of which are roughly $10 \times 10 \times 30$ cm), the source term for ^{182}Ta gamma-rays from a TS-1 target is spread over a volume of ~ 3 litres). Of course, gamma-ray emission probabilities are rarely 100%, but these emission probabilities may be looked up in tables [4], copied off the web [5], or downloaded as decay files [6].

Absorption of gamma-rays between the source and the detector may be written as $\prod_j \exp(-(\mu/\rho(k))_j \rho_j r_j)$ where the $\exp(-(\mu/\rho(k))_j \rho_j r_j)$ ’s are the attenuation factors in the absorbing materials j between the source and the detector, $(\mu/\rho(k))_j$ is the mass attenuation coefficient for gamma-rays of energy k in material j , ρ_j is the density of material j , and r_j is the distance travelled by the gamma-ray in material j . Mass attenuation coefficients may be looked up in printed tables [7], copied from the web [8] or downloaded from databases [9] (see Appendix 2 about whether or not to include coherent scattering). For sufficiently thick shields, energy dependences of attenuation factors can be large; although the difference between the mass attenuation coefficients μ/ρ for lead at the two ^{60}Co gamma-ray energies of 1173 and 1332 keV may be only 9%, in $r_j = 17$ cm of lead (the thickness of lead (density 11.3 g cm^{-3}) in the flask wall), the difference between the corresponding attenuation factors $\exp(-(\mu/\rho(k))_j \rho_j r_j)$ is a factor² ~ 3 .

Full-energy-peak detection efficiencies for HPGe gamma-ray detectors may be measured using calibration sources [10], deduced from manufacturers’ measured data [11], or taken from systematics [12]. For source-to-detector distances large compared with the dimensions of the germanium crystal, the efficiency varies as $1/R^2$ where R is the source-to-detector distance.

In the present report, the measured gamma-ray spectra were analysed in two ways, one (‘by division’) essentially by dividing count rates by products of emission probability, attenuation factors and detection efficiency, the other (‘by fitting’) by exploiting the dependence on gamma-ray energy of gamma-ray mass attenuation coefficients by fitting count rates of gamma-ray lines from radionuclides emitting several lines suitably spaced in gamma-ray energy. In the latter case, the essence of the method is to fit $c(k) = \alpha(k) \exp(-\mu/\rho(k) \rho t) \varepsilon(k) a$ ($c(k)$ = count rate, $\alpha(k)$ = emission probability, $\varepsilon(k)$ = detection efficiency) at the energies $k = k_i$ of visible gamma-ray lines to the corresponding measured count rates C_i with thickness ρt and activity a as parameters, by minimising $\chi_{\text{pdf}}^2 = (\sum_i (C_i - c(k_i))^2 / (\delta C_i)^2) / (n - 2)$ where n is the number of gamma-ray lines fitted. (For fitting count rates from the measured gamma-

² Consequently, for example, although as they appear in a gamma-ray spectrum the two ^{60}Co lines usually have similar strengths, outside such a thick-lead-walled flask the strength of the higher-energy gamma-ray line is noticeably greater than the strength of the lower-energy line.

ray spectra described in Sect. 5, the minimisation routine VA04A [13] was used³.) Uncertainties in the fitted parameters can be established by repeatedly (*e.g.* 100 times) perturbing count rates C_i by amounts randomly chosen from gaussian distributions with standard deviations δC_i where δC_i is the uncertainty in C_i and refitting, and then taking standard deviations of the sets of ‘perturbed’ parameter values. However, this latter method fails either if the energies of the gamma-ray lines that are fitted do not span a sufficiently wide range of energies, or if the statistics on the measured count rates are too poor, as the parameters ρt and a are highly correlated⁴.

The ‘fitting’ method set out in the preceding paragraph implicitly assumed one source of gamma-rays and one absorber thickness. But if there is ‘structure’ in the source term (such as the activity in the cylindrical body of a TS-2 target inside its ~1-inch-thick steel sleeve (see Fig. A1 in Appendix 1) and the activity in the flange at the back of the target outside the sleeve), it may be necessary to extend the method to two sources of gamma-rays and two absorber thicknesses whereupon the function to be fitted becomes $c(k) = \alpha(k) \exp(-\mu/\rho(k) \rho t_1) \varepsilon(k) a_1 + \alpha(k) \exp(-\mu/\rho(k) \rho t_2) \varepsilon(k) a_2$.

4. Activity calculations

MCNPX models of the ISIS Target Stations have been built using the CombLayer tool [14]. This tool (a set of C++ programs) was created by Stuart Ansell⁵ during his work on a neutronics model of the ISIS Second Target Station (TS-2). The initial idea behind the creation of this tool was to overcome significant limitations in the process of defining complex models (geometries) within the MCNP(X) Monte Carlo code (see [14] for more details). Within CombLayer, the user is required to write the model geometry into the C++ construction system. This is then compiled into the final program which, after running, produces the MCNPX input file. This object-oriented approach allows rapid production of complex MCNPX models where the majority of engineering details can be described in detail. The global database of all variables (positions and dimensions of objects, and specifications of the materials that make up the objects) in CombLayer makes it easy to make changes without fearing that the model will become broken. In addition to this, the path-tracking routines in MCNPX can be dramatically accelerated by optimising the model within CombLayer (*i.e.* by reducing the number of unique surfaces). After the model geometry has been constructed, additional processing can be applied to define source terms and tallies. For the calculations described in this report, a sub-set of C++ programs was dedicated to the preparation of the neutron tallies and other files (and data) needed for subsequent runs of the transmutation code.

The work on CombLayer was, for a significant amount of time, a ‘one-man’ project. However, with the initiation of the feasibility phase of the ISIS TS-1 Project [2] in 2011, the CombLayer code has been extended, modified and improved by other members of the ISIS neutronics team, and CombLayer reached the size of hundreds of thousands of lines of C++ code in the period between 2012 and 2016. As a result of this work more than 160 Monte Carlo models of the modified ISIS Target Station 1 (TS-1) have been created, tested and analysed with the idea of finding the optimal design of the future

³ VA04A is identical to VA24A, except that instead of working space having to be made available in common storage, working space is passed to the routine as an argument.

⁴ The sides of the χ^2_{pdf} ‘valley’ may be steep, but the depth of the floor varies but slowly along the length of the valley.

⁵ Currently at MAX IV Laboratory, Lund, Sweden.

ISIS TS-1 [2, 15, 16]. CombLayer is an open-source tool [17], and today there are many contributors who are developing CombLayer and expanding it to cover the models of different neutron production facilities around the world. It should be noted here that the ISIS neutronics team has its own, independent version of the code which is used to produce the models of ISIS Target Stations.

The MCNPX model of TS-1 incorporates 3100 objects (volumes) and 3500 unique surfaces. It is defined by 4300 parameters (dimensions, positions, *etc.*) and includes detailed description of seventeen materials (this includes the fractions of each stable isotope in the elements making up the materials). The basic model of TS-2 incorporates 1400 objects, 1600 unique surfaces, 1500 parameters and fifteen materials. When the detailed descriptions of the ZOOM, ChipIr and IMAT neutron beam-lines on ISIS are included, these numbers will be increased by a factor of 3.

Activity calculations for the ISIS targets were carried out using the Monte Carlo codes MCNPX 2.70, HTAPE3X and CINDER-90 [3, 18]. The CEM03 physics model [19] and ENDF/B-VII cross-section library [20] were used, and MCNPX was forced to use tables (if available) for neutron interactions up to the CINDER-90 upper limit of 25 MeV.

It has to be noted that for the activity calculations related to the ISIS targets ‘reduced’ models have been used. This means that the bulk shielding and beam-line details have been excluded and that only the target, moderators and reflector (including moderator pipes, decouplers, flight-path liners, *etc.*) have been used. This reduces the numbers of objects, unique surfaces and parameters in the MCNPX models from a few thousands to a few hundred. Even with reduced geometry and optimized MCNPX particle tracking the run-times for the models are significant. As an illustration, the average amount of time to calculate particle histories initiated by a single incoming particle is 0.16 seconds on quite a powerful personal workstation (under the Linux operating system). Also, the size of the output file is 0.5 kB per event per object in the model geometry. Transmutation code calculations are much faster. What is needed for them is a reasonably accurate record of the irradiation time profile. To control the execution of the transmutation code calculations and post-processing of obtained results a set of in-house Bash shell scripts has been created.

5. Activities extracted from gamma-ray spectra

5.1 TS-1 W#2 target

Gamma-ray spectrum measurements outside RAL’s transport flask⁶ containing the TS-1 W#2 target were made on 10 November 2016 in the TSA2 service tunnel in Building R80 at RAL. With the target oriented nose-down in the flask and the axis of the flask vertical, a gamma-ray spectrum at a distance of 50 cm from the outside of the flask at the height of the target was measured using a Canberra Falcon 5000 spectrometry system incorporating an HPGe gamma-ray detector with a BE2830 crystal (28 cm² nominal area, 3.0 cm nominal thickness); the measurement time was 4 hours, and the dead-time was 2.2%. Two ⁶⁰Co and six ¹⁷²Lu lines were fitted as described in Sect. 3 to extract activities of ⁶⁰Co and ¹⁷²Lu assuming one gamma-ray source and one

⁶ Basic dimensions of transport flask: cavity diameter 605 mm; cavity steel wall thickness 6 mm; lead thickness 167.5 mm; flask outer steel wall thickness 16 mm dimensions; flask outer diameter 984 mm.

absorber. The lines fitted are given in Table 2, results are given in Table 3, and full details are given in [21].

5.2 TS-1 W#3 target

Gamma-ray spectrum measurements outside a storage flask⁷ containing the TS-1 W#3 target were made between 22 and 28 May 2019 in Building R105 at RAL. With the target oriented nose-down in the flask and the axis of the flask vertical, gamma-ray spectra were measured with two HPGe gamma-ray detectors, a Canberra BE3825 detector (38 cm² nominal area, 2.5 cm nominal thickness, operated with Canberra's 2-inch 90° collimation system in place) and the Canberra BE2830 detector (see Sect. 5.1) both positioned 100 cm from the surface of the flask; the heights of the HPGe detectors above the floor corresponded to within ~2 cm with the midpoint of the 38.7-cm-long target core, and the azimuthal angle between the lines from the axis of the flask to the detectors was 90°. Spectra were accumulated over 2–3 days, and dead times ranged between 7 and 10%. To extract activities, two ⁶⁰Co lines were fitted assuming one gamma-ray source and one absorber, and seventeen ¹⁷²Lu lines (see Table 2) were fitted as described in Sect. 3 assuming two gamma-ray sources and two absorbers. The results for ⁶⁰Co and ¹⁷²Lu are given in Table 3, and full details are given in [22]. The activity of ¹⁸²Ta in the target was also extracted, in this case by dividing count rates by products of emission probability, attenuation factors and detection efficiency, assuming the known geometry of the tantalum component of the target core. The result for ¹⁸²Ta is also given in Table 2, and full details are given in [23].

⁷ Basic dimensions of storage flasks: cavity diameter 552 mm; cavity steel wall thickness 6 mm; lead thickness 170 mm; flask outer steel wall thickness 15 mm; flask outer diameter 934 mm. Storage flasks are also used as transfer flasks.

Line, keV	TS-1 W#2	TS-1 W#3	TS-2 W#1+2+3	TS-2 W#6+7+8
⁶⁰ Co				
1173	•	•		
1332	•	•		
¹⁷² Lu				
1094	•	•	•	•
1387		•	•	
1398			•	
1403		•	•	•
1440		•	•	•
1461			•	
1466		•	•	
1470		•	•	
1489	•	•	•	•
1543	•	•	•	
1584	•	•	•	
1602		•	•	
1609			•	
1622	•	•	•	
1670		•	•	
1724		•	•	
1813		•	•	
1915	•	•	•	
1994		•	•	
2025		•	•	
¹⁸² Ta				
1121		•		
1189		•		
1221		•		
1231		•		
1257				•

Table 2. Gamma-ray lines used as described in Sect. 3 in order to extract activities.

5.3 TS-2 W#1, W#2 and W#3 targets

Gamma-ray spectrum measurements outside the transport flask containing the three TS-2 targets W#1, W#2 and W#3 were made between 10 and 14 August 2017. Inside the flask the three targets were held nose-down with their axes vertical, and with the target axes spaced at 120° intervals on a circle of radius 140 mm centred on the vertical axis of the flask. Several gamma-ray spectra were recorded with the Canberra BE2830 HPGe detector 50 cm from the surface of the cylindrical flask, the longest being 65 hours; dead times were less than 1%. In order to obtain realistic results from fitting twenty ¹⁷²Lu lines (see Table 2), it was found necessary to assume two gamma-ray sources and two absorbers, the smaller absorber thickness corresponding to the flanges at the back of the targets, and the larger absorber thickness corresponding to the cores of the targets inside their ~1-inch-thick steel sleeves. The result is given in Table 3, and full details are given in [24].

5.4 TS-2 W#6, W#7 and W#8 targets

Gamma-ray spectrum measurements outside a storage flask containing the three TS-2 targets W#6, W#7 and W#8 were made between 16 and 19 December 2019. The arrangement of the three targets inside the flask was exactly the same as the arrangement for the TS-2 W#1–3 targets described in Sect. 5.3. Several gamma-ray spectra were recorded using two HPGe gamma-ray detectors, the Canberra BE3825 (operated with Canberra’s 2-inch-thick 90° lead collimator in place) and the Canberra BE2830, the longest being 48 hours. The two detectors were positioned around the flask 90° apart, and distances between the BE3825 and BE2830 detectors and the vertical flask axis were 347 cm and 167 cm respectively; dead times were less than 1%. Extraction of activities was difficult, essentially because the orientation of the set of three targets inside the flask relative to the HPGe detectors was not known, but the procedure used is fully described in Appendix 1 of the present report, and the results therefrom are given in Table 3 (and the gamma-ray lines used are given in Table 2).

Target		TBq, meas.	TBq, calc.	Method	Ref.
TS-1 W#2	⁶⁰ Co	0.099 ± 0.015	0.087	F(1)	[21]
	¹⁷² Lu	0.842 ± 0.315	0.791	F(1)	
TS-1 W#3	⁶⁰ Co	0.55 ± 0.15	0.18	F(2)	[22]
	¹⁷² Lu	2 ± 1	3.1	F(2)	
	¹⁸² Ta	0.136 ± 0.026	0.163 ± 0.012	D	[23]
TS-2, W#1, 2, 3	¹⁷² Lu	0.350 ± 0.080	0.425 ± 0.085	F(2)	[24]
TS-2, W#6, 7, 8	¹⁷² Lu	3 ± 1	2.8	D	App. 1
	¹⁸² Ta	61 ± 9	86	D	

Table 3. Comparison between activities deduced from gamma-ray spectrum measurements and activities calculated using Monte Carlo computer codes. In the ‘Method’ column, F(*n*) denotes that the activity was obtained by fitting *n* sources as described in Sect. 3; D denotes that the activity was obtained by division of the count rate, as also described in Sect. 3.

6. Discussion

How should these various results be summarised? Since it is of interest to attempt to derive some overall measure of how well measurement and calculation agree, Table 4 sets out single numbers for the eight pairs of measured and calculated activities presented in Table 3. In view of the difficulty in assigning ‘accurate’ values of uncertainty to each of the measured and calculated values, the approach being taken here for averaging is simply to regard all eight measurement ÷ calculation quotients as having the same weight. Whilst it is obviously doubtful whether the quotients are distributed according to the classical normal distribution, nevertheless it is reasonably clear that on average agreement between the results of measurements and the results of Monte Carlo calculations is good to within 20–30%, consistent with the expected limitation due to uncertainties pointed out in Sect. 1.

This encouraging agreement is also consistent with the findings of decay heat⁸ measurements and calculations. Three exercises to measure decay heat in ISIS TS-1

⁸ Thermal power dissipation within a target after beam switch-off.

targets have been carried out, in November 2016, March 2018, and December/January 2018/2019. The overall conclusions from these measurements and calculations [29, 30] are, respectively, that ‘decay heats deduced from the measurements agree well with decay heat calculations using the Monte Carlo computer code MCNPX’, and that ‘the Monte Carlo code MCNPX is a reliable predictor of decay heat’.

	Measurement ÷ calculation
Mean	1.17
Standard deviation	0.73
Standard error	0.26

Table 4. Overall comparison between activities in irradiated ISIS targets measured by gamma-ray spectrometry and activities calculated using Monte Carlo computer codes. All eight measurement ÷ calculation quotients have been assumed to have the same weight.

7. Conclusions

The essential conclusion from four exercises to extract radionuclide activities from gamma-ray spectrum measurements (and also from exercises to measure decay heat) is that the measured results agree with results calculated using the Monte Carlo MCNPX + HTAPE3X + CINDER-90 codes to within 20–30%, which is as good agreement as can realistically be expected.

Overall, this is a very encouraging conclusion.

References

- [1] <https://www.isis.stfc.ac.uk>.
- [2] G P Škoro *et al.*, *Physica B: Condens. Matter*. 551 (2018) 381–385.
- [3] MCNPX 2.7.0 — Monte Carlo N-Particle Transport Code System for Multi-Particle and High-Energy Applications, <https://mcnpx.lanl.gov/>.
- [4] Catalogue of Gamma Rays from Radioactive Decay, U Reus and W Westmeier, *Atom. Data Nucl. Data Tables*, 29 (1983) 193–406.
- [5] <https://www-nds.iaea.org/relnsd/NdsEnsdf/QueryForm.html>.
- [6] <http://www.nndc.bnl.gov/ensdf/b7.1/download.html>.
- [7] For example, *Photon Cross Sections, Attenuation Coefficients, and Energy Absorption Coefficients from 10 keV to 100 GeV*, J H Hubbell, NSRDS-NBS 29 (1969).
- [8] For example, <https://www.nist.gov/pml/x-ray-mass-attenuation-coefficients>.
- [9] For example, <https://www.nist.gov/pml/xcom-photon-cross-sections-database>.
- [10] For example, from Eckert and Ziegler, <https://www.ezag.com/home/>.
- [11] For example, <https://www.mirion.com/products/s573-isocs-calibration-software>.

- [12] D J S Findlay, *Radiat. Meas.* 94 (2016) 23.
- [13] Harwell Subroutine Library, <http://hsl.rl.ac.uk/>.
- [14] S Ansell, Proc. ICANS XXI Meeting, Mito, Japan, 2014, JAEA-Conf. 2015-002, p 148–154.
- [15] G P Škoro and S Ansell, Proc. ICANS XXI Meeting, Mito, Japan, 2014, JAEA-Conf. 2015-002 (2016) p 141–147.
- [16] G P Škoro *et al.*, Internal Report ISIS-TS1-UPG-NEU-Rp-0001, September 2016.
- [17] <https://github.com/SAnsell/CombLayer>.
- [18] W L Wilson *et al.*, Proc. SARE4 Workshop, Knoxville, USA, 1998.
- [19] S G Mashnik *et al.*, *J. Phys.: Conference Series* 41 (2006) 340–351. doi:10.1088/1742-6596/41/1/037.
- [20] M B Chadwick *et al.*, *Nucl. Data Sheets* 112 (2011) 2887.
- [21] D J S Findlay, G P Škoro, G J Burns, S Ansell, *Appl. Radiat. Isot.* 125 (2017) 1–3.
- [22] D J S Findlay, ISIS report ISIS/WR/2019/02 (ISIS-DJSF-19-06-B), 2019.
- [23] G P Škoro, D J S Findlay, G J Burns, *Nucl. Instr. Meth. A* 961 (2020) 163641.
- [24] D J S Findlay, G P Škoro, G J Burns, *J. Radiol. Prot.* 38 (2018) N36–N43.
- [25] D J S Findlay, ISIS internal report ISIS-DJSF-20-01-A, 20 January 2020.
- [26] D J S Findlay, ISIS internal report ISIS-DJSF-20-01-C, 30 January 2020.
- [27] N P Taylor and J Needham, ‘MORSE-H: A Revised Version of the Monte Carlo Code MORSE’, AERE-R 10432, 1982.
- [28] L J Baker and N P Taylor, ‘The Harwell Version of the DLC37F Nuclear Data Library’, AERE-R 11849, 1985.
- [29] D J S Findlay *et al.*, *Nucl. Instr. Meth.* A908 (2018) 91–96.
- [30] G M Allen *et al.*, *Nucl. Instr. Meth.* A933 (2019) 8–11.

Appendix 1 — Activities of ^{172}Lu and ^{182}Ta I TS-2 targets W#6+7+8

In [25] an analysis was presented of gamma-ray spectrometry measurements made on a storage flask containing the three spent ISIS TS-2 targets W#6, W#7 and W#8 (see Table 1 in the main body of the text). The analysis was based on the technique described in Sect. 3 of exploiting the dependence on gamma-ray energy of gamma-ray mass attenuation coefficients by fitting count rates of gamma-ray lines from radionuclides emitting several lines suitably spaced in gamma-ray energy. However, the uncertainties in the activities of ^{172}Lu and ^{182}Ta deduced thereby were large — not helped by the fact that the orientation of the set of three targets inside the flask relative to the two HPGe detectors outside the flask was not known. In the present appendix, which is a revised version of [26], the orientation of the set of three targets inside the flask is deduced, and then the measured detector count rates are divided by products of gamma-ray emission probabilities, attenuation factors, and gamma-ray detection efficiencies in order to obtain estimates of activity.

Two HPGe gamma-ray detectors were used in the measurements, the Canberra BE3825 (operated with Canberra's 2-inch-thick 90° lead collimator in place) and the Canberra BE2830 already referred to in the main body of the text. The two detectors were positioned around the flask 90° apart in a manner similar to the arrangement shown in Fig. 3, and distances between the BE3825 and BE2830 detectors and the vertical flask axis were 347 cm and 167 cm respectively. Table A1 compares the full-energy-peak detection efficiencies [12] $\varepsilon = \varepsilon(k)$ for the two detectors (where k is the gamma-ray energy). It is evident that between 1000 and 2000 keV (the range of gamma-ray energies of relevance in the present work) the ratio of detection efficiencies can be taken as being constant at 0.251 to within $\pm 1\%$. In [25], it was shown that the average ratios of detector count rates were as given in Table A2, from which, in combination with the efficiency ratios given in Table A1, it is evident that the ^{172}Lu activities seen by the two HPGe detectors are similar, whereas the BE3825 detector is seeing $\sim 3.1 \div 0.251 = \sim 12\text{--}13$ times as much ^{182}Ta as the BE2830 detector — and these ratios of activities seen by the two detectors are also given in Table A2.

keV	ε , BE3825 (coll.) at 347 cm	ε , BE2830 at 167 cm	ε BE3825 $\div \varepsilon$ BE2830
1000	1.99E-06	7.81E-06	0.2548
1200	1.65E-06	6.52E-06	0.2531
1400	1.41E-06	5.60E-06	0.2518
1600	1.23E-06	4.91E-06	0.2505
1800	1.09E-06	4.37E-06	0.2494
2000	9.76E-07	3.94E-06	0.2477

Table A1. Comparison of full-energy-peak detection efficiencies for the two HPGe gamma-ray detectors. Because of the surrounding collimator, the effective area presented by the BE3825 crystal is reduced⁹ from a nominal 38 cm^2 to 33.8 cm^2 . Within the energy range shown, the ratio of detection efficiencies can be taken as being constant at 0.251 to within $\pm 1\%$.

⁹ The effective area of the crystal with the 90° collimator in place (half-angle 45°) is $\int_0^{r_{\text{coll}}} 2\pi r dr + \int_{r_{\text{coll}}}^{r_{\text{xtal}}} \exp(-\mu/\rho \rho(r - r_{\text{coll}})) 2\pi r dr$ where r_{coll} is the radius of the 'tip' of the tapered collimator aperture, μ/ρ is the gamma-ray mass attenuation coefficient for lead, ρ is the density of lead, and r_{xtal} is the radius of the HPGe crystal.

	BE3825 count rate ÷ BE2830 count rate	Activity seen by BE3825 ÷ activity seen by BE2830
¹⁷² Lu	~0.25	~1
¹⁸² Ta	~3.1	~12–13

Table A2. Average ratios of count rates from the two HPGe detectors, and, by dividing by the ratio of detection efficiencies (Table A1), ratios of activity seen by the two detectors.

In order to try to understand the two different apparent activity ratios of ~1 (for ¹⁷²Lu) and ~12–13 (for ¹⁸²Ta), the angular distribution of gamma-rays outside the flask relative to an *assumed* orientation of the set of three gamma-ray-emitting targets inside the flask inside the flask was calculated. The arrangement of targets inside the flask is shown schematically in Fig. A1. The Monte Carlo computer code MORSE [27] in point-detector mode was used to represent the three targets inside the flask and to compute the angular distribution of ‘uncollided flux¹⁰’ per source gamma-ray outside the flask $\prod_j \exp(-\mu_j r_j)/(4\pi R^2)$ where R is the source-to-point-detector distance, and the $\exp(-\mu_j r_j)$ ’s are the attenuation factors in the absorbing materials between the source and the point detector. Gamma-rays were represented by group 117 (1000–1500 keV) of the Harwell version [28] of the coupled-neutron-gamma 121-group-cross-section DLC37F library. For each target, the source density of ¹⁷²Lu gamma-rays within the cylindrical target core was assumed to vary linearly with ρ whilst going to zero at the surface of the target core¹¹ and uniform in ϕ and z where ρ , ϕ and z are the conventional cylindrical polar coordinates representing the target core, and the source density of ¹⁷²Lu gamma-rays within the flange at the back of the target was taken to be uniform. Also, for each target, the source density of ¹⁸²Ta gamma-rays in the target core was assumed to be concentrated in the outermost 5 mm of the target core, in line with the location of the tantalum cladding (see Fig. 2), and the source density of ¹⁸²Ta gamma-rays within the flange at the back of the target was taken to be uniform. The relative numbers for the source strengths were taken from MCNPX calculations, and are given in Table A3. The resultant angular distributions are given in Fig. A2 and in Table A4.

Is it possible to see in the two curves $S = S(\theta)$ in Fig. A2 an explanation for the observed ratios of count rates shown in Table A2? The two HPGe detectors are spaced 90° apart, and since clockwise rotation around the flask as seen from above corresponds to increasing angles, the BE2830 detector is 90° ‘behind’ the BE3825 detector. Consequently, the question becomes: is there an angle θ where $S(\theta) \cong 13 S(\theta - 90^\circ)$ for ¹⁸²Ta and $S(\theta) \cong S(\theta - 90^\circ)$ for ¹⁷²Lu? From Table A4, wherein are set out the numbers behind Fig. A2, the answer would appear to be yes, for $\theta \cong 50^\circ$. Consequently, for ¹⁷²Lu and ¹⁸²Ta the uncollided fluxes at the position of the BE3825 detector were taken respectively as $(5.3 \pm 0.5) \times 10^{-14}$ and $(1.60 \pm 0.16) \times 10^{-13} \text{ cm}^{-2} \text{ s}^{-1}$ per source gamma-ray per second.

¹⁰ The flux of the very few gamma-rays that have not been absorbed and not been scattered by the time they pass through the outer skin of the flask.

¹¹ Since 6.7-day ¹⁷²Lu is in equilibrium with 1.87-year ¹⁷²Hf, since (for example) the TENDL-2019 cross-section for ¹⁸⁴W(p, x)¹⁷²Hf increases monotonically up to the 200-MeV high-energy limit of the TENDL tabulations [https://tendl.web.psi.ch/tendl_2019/tendl2019.html], and since high-energy protons within the target tend to be concentrated towards the central axis, the distribution of ¹⁷²Lu nuclei will be concentrated towards the central axis.

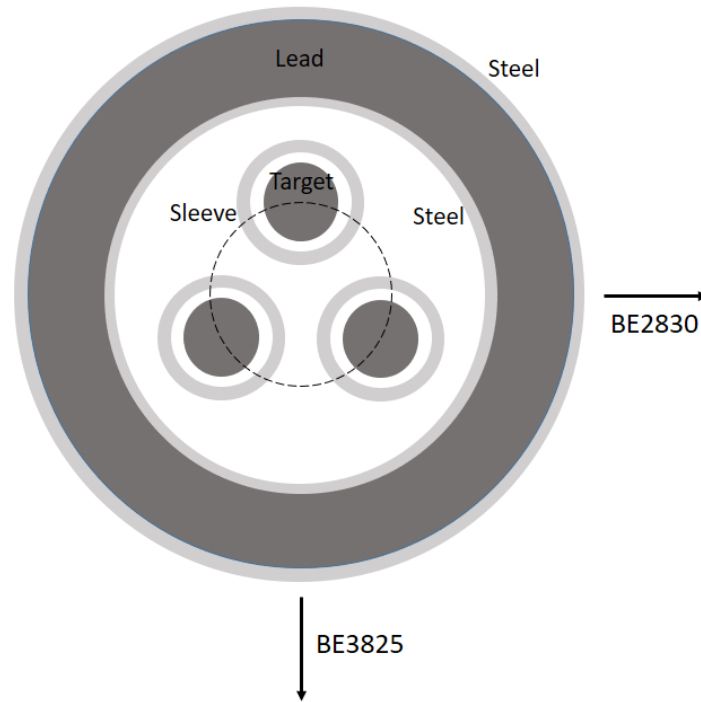


Fig. A1. Schematic arrangement, not to scale, of three targets inside the storage flask, looking vertically. Dimensions (from outside going inward): outer flask steel skin 15 mm; lead 170 mm; inner steel skin 6 mm; 3 × stainless-steel sleeves 26 mm thick; targets centred on 140-mm radius circle. The targets are held nose-down; the cylindrical tantalum-clad tungsten target bodies are held inside the sleeves, but the tantalum flanges at the back of the targets lie just above the top of the sleeves. Relative orientations of the two HPGe detectors are shown.

TS-2 target	^{172}Lu		^{182}Ta	
	Core	Flange	Core	Flange
W#6	0.2098	0.0002	0.0187	0.0013
W#7	0.9592	0.0008	1.361	0.099
W#8	1.6387	0.0013	78.14	5.57

Table A3. *Relative strengths of gamma-ray sources in targets* (taken from MCNPX + HTAPE3X + CINDER-90 Monte Carlo calculations). Note that the corresponding numbers for the ^{172}Lu and ^{182}Ta source strengths are *not* related to each other.

Angle	Uncoll. flux, ¹⁷² Lu	Uncoll. flux, ¹⁸² Ta	¹⁷² Lu, $S(\theta) \div$ $S(\theta - 90^\circ)$	¹⁸² Ta, $S(\theta) \div$ $S(\theta - 90^\circ)$
0.00	8.08E-14	3.17E-13	1.45	2.25
3.75	7.99E-14	3.16E-13	1.39	2.23
7.50	7.87E-14	3.09E-13	1.32	2.16
11.25	7.18E-14	2.45E-13	1.16	1.67
15.00	5.60E-14	1.85E-13	0.86	1.22
18.75	3.71E-14	1.22E-13	0.54	0.78
22.50	2.39E-14	5.19E-14	0.33	0.32
26.25	2.14E-14	1.04E-14	0.29	0.06
30.00	2.13E-14	3.54E-15	0.28	0.02
33.75	2.17E-14	4.43E-15	0.28	0.02
37.50	2.28E-14	9.98E-15	0.30	0.06
41.25	2.73E-14	4.66E-14	0.40	0.37
45.00	3.80E-14	8.35E-14	0.69	0.96
48.75	5.05E-14	1.20E-13	1.15	2.41
52.50	5.85E-14	1.60E-13	1.52	12.14
56.25	5.92E-14	1.82E-13	1.63	24.62
60.00	5.84E-14	1.74E-13	1.70	27.79
63.75	5.79E-14	1.66E-13	1.75	12.98
67.50	5.65E-14	1.59E-13	1.65	2.96
71.25	5.09E-14	1.52E-13	1.11	1.23
75.00	4.29E-14	1.46E-13	0.68	0.79
78.75	3.60E-14	1.41E-13	0.47	0.57
82.50	3.28E-14	1.38E-13	0.40	0.44
86.25	3.19E-14	1.36E-13	0.39	0.43
90.00	3.13E-14	1.35E-13	0.39	0.43
93.75	3.13E-14	1.36E-13	0.39	0.43
97.50	3.29E-14	1.38E-13	0.42	0.45
101.25	4.10E-14	1.43E-13	0.57	0.58
105.00	5.24E-14	1.48E-13	0.93	0.80
108.75	6.22E-14	1.55E-13	1.68	1.27
112.50	6.69E-14	1.63E-13	2.80	3.13
116.25	6.85E-14	1.71E-13	3.21	16.52
120.00	7.02E-14	1.81E-13	3.30	51.05
123.75	7.19E-14	1.92E-13	3.30	43.28
127.50	7.36E-14	2.04E-13	3.23	20.42
131.25	7.22E-14	2.16E-13	2.65	4.64
135.00	6.56E-14	2.29E-13	1.73	2.75
138.75	5.73E-14	2.44E-13	1.13	2.03
142.50	5.23E-14	2.58E-13	0.89	1.61
146.25	5.36E-14	2.74E-13	0.91	1.50
150.00	5.64E-14	2.90E-13	0.96	1.66
153.75	5.93E-14	3.05E-13	1.02	1.84
157.50	6.24E-14	3.20E-13	1.10	2.02
161.25	6.72E-14	3.34E-13	1.32	2.20
165.00	7.53E-14	3.46E-13	1.76	2.37
168.75	8.41E-14	3.56E-13	2.34	2.52
172.50	8.98E-14	3.64E-13	2.74	2.65
176.25	9.07E-14	3.69E-13	2.85	2.72
180.00	9.02E-14	3.70E-13	2.88	2.74
183.75	8.93E-14	3.68E-13	2.85	2.71
187.50	8.77E-14	3.64E-13	2.66	2.63
191.25	8.47E-14	3.57E-13	2.07	2.50
195.00	8.09E-14	3.47E-13	1.54	2.34

198.75	7.70E-14	3.35E-13	1.24	2.17
202.50	7.37E-14	3.22E-13	1.10	1.98
206.25	7.07E-14	3.07E-13	1.03	1.80
210.00	6.77E-14	2.92E-13	0.96	1.61
213.75	6.48E-14	2.76E-13	0.90	1.44
217.50	6.24E-14	2.60E-13	0.85	1.27
221.25	6.15E-14	2.44E-13	0.85	1.13
225.00	6.15E-14	2.29E-13	0.94	1.00
228.75	6.14E-14	2.15E-13	1.07	0.88
232.50	6.05E-14	2.01E-13	1.16	0.78
236.25	5.91E-14	1.89E-13	1.10	0.69
240.00	5.82E-14	1.79E-13	1.03	0.62
243.75	5.76E-14	1.69E-13	0.97	0.55
247.50	5.73E-14	1.61E-13	0.92	0.50
251.25	5.66E-14	1.54E-13	0.84	0.46
255.00	5.52E-14	1.49E-13	0.73	0.43
258.75	5.36E-14	1.45E-13	0.64	0.41
262.50	5.30E-14	1.42E-13	0.59	0.39
266.25	5.41E-14	1.41E-13	0.60	0.38
270.00	5.57E-14	1.41E-13	0.62	0.38
273.75	5.75E-14	1.41E-13	0.64	0.38
277.50	5.95E-14	1.43E-13	0.68	0.39
281.25	6.20E-14	1.47E-13	0.73	0.41
285.00	6.54E-14	1.51E-13	0.81	0.43
288.75	6.88E-14	1.56E-13	0.89	0.47
292.50	7.17E-14	1.63E-13	0.97	0.50
296.25	7.36E-14	1.70E-13	1.04	0.55
300.00	7.51E-14	1.78E-13	1.11	0.61
303.75	7.64E-14	1.86E-13	1.18	0.68
307.50	7.59E-14	1.65E-13	1.22	0.63
311.25	6.78E-14	1.24E-13	1.10	0.51
315.00	5.51E-14	8.73E-14	0.90	0.38
318.75	4.38E-14	5.00E-14	0.71	0.23
322.50	3.84E-14	1.32E-14	0.63	0.07
326.25	3.62E-14	7.41E-15	0.61	0.04
330.00	3.45E-14	6.27E-15	0.59	0.04
333.75	3.31E-14	1.28E-14	0.58	0.08
337.50	3.42E-14	5.37E-14	0.60	0.33
341.25	4.59E-14	1.23E-13	0.81	0.80
345.00	6.31E-14	1.86E-13	1.14	1.24
348.75	7.70E-14	2.46E-13	1.44	1.70
352.50	8.22E-14	3.10E-13	1.55	2.18
356.25	8.16E-14	3.16E-13	1.51	2.24
360.00	8.08E-14	3.17E-13	1.45	2.25

Table A4. Angular distributions $S = S(\theta)$ of uncollided flux per source gamma-ray per second outside the flask at 347 cm from the axis of the flask for 1000–1500-keV source gamma-rays, and ratios of these fluxes spaced by 90°. The ratios representing the best match to the observed ratios are highlighted in bold text.

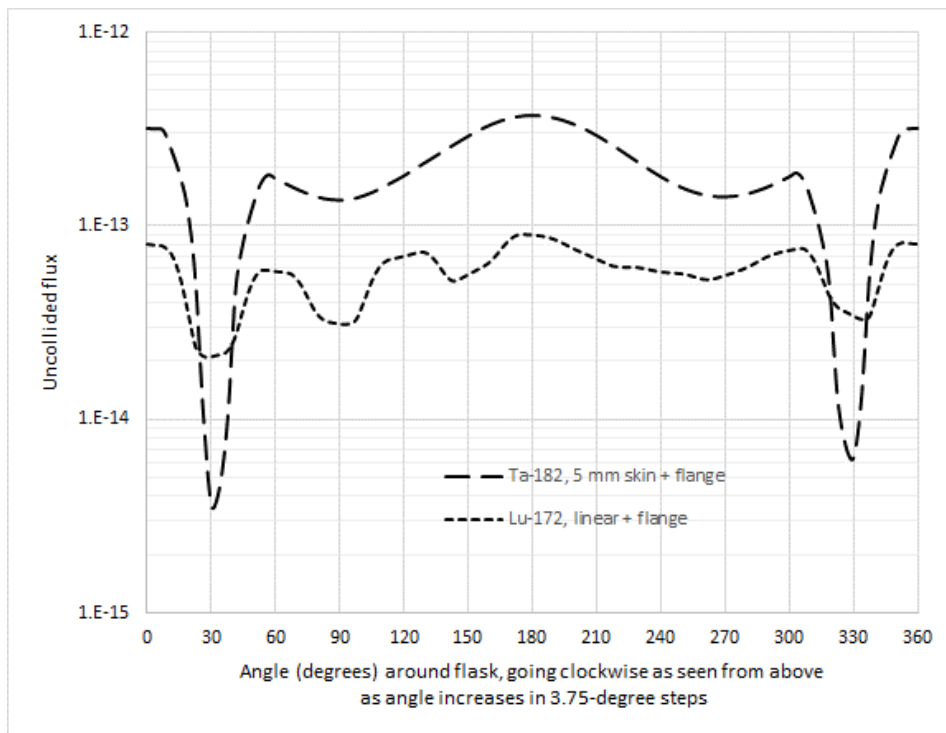
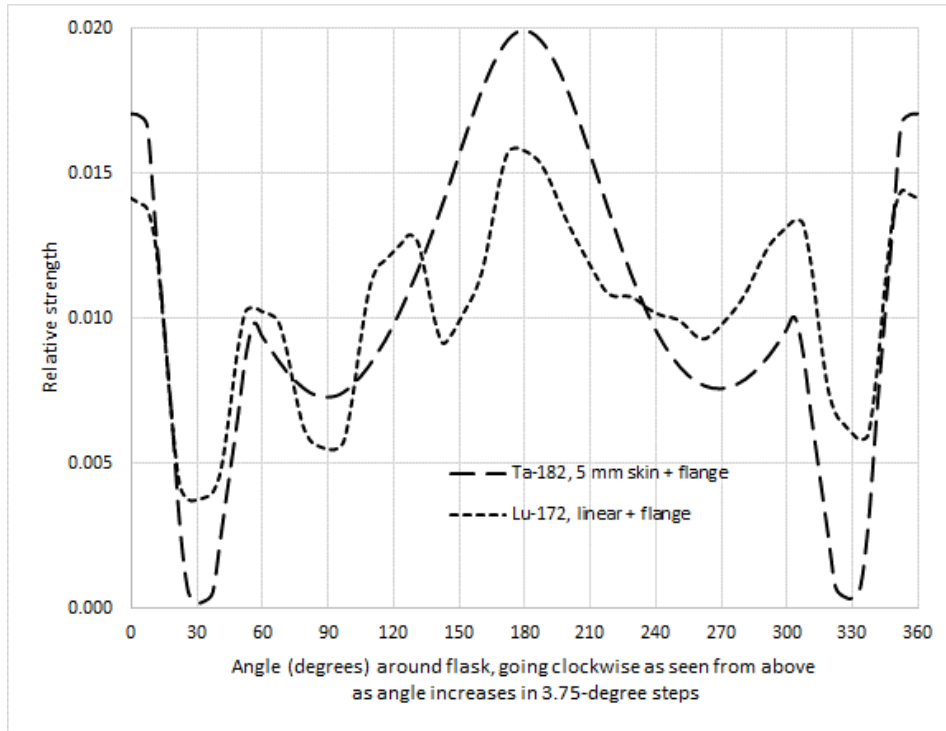


Fig. A2. Angular distributions $S = S(\theta)$ of uncollided flux per source gamma-ray per second at 347 cm from flask axis of 1000–1500-keV gamma-rays outside the flask, where, in Fig. A1, 0° corresponds to the angular position of the arrow pointing to the BE3825 detector with the highest-activity target uppermost as shown in the figure. The ‘relative strength’ vertical axis is $S(\theta_i)/\sum_i S(\theta_i)$ with θ_i in 3.75° steps. The shapes are not overly sensitive to realistic variations in representation of source spatial distributions. The ^{182}Ta curve is essentially symmetric about 180° because the ^{182}Ta activity in two of the targets is essentially negligible in comparison with the ^{182}Ta activity in the highest-activity target, whereas the ^{172}Lu curve is less symmetric because the activities in all three targets are not so very different.

In principle, activities A_i of ^{172}Lu and ^{182}Ta can now be obtained by dividing observed count rates C_i for gamma-ray lines i by products of gamma-ray emission probabilities α_i , attenuation factors η_i and detection efficiencies ε_i . But since attenuation factors within source material and shielding have been computed using group cross-sections, from which gamma-ray lines should activities be extracted?

For ^{182}Ta , the 1257-keV line is nearest the centre of the 1000–1500-keV energy group for which the group cross-section for lead is 19.73 barns. The cross-sections from the NIST XCOM database [9] for Pb at 1257 keV are 20.13 barns including coherent (Rayleigh) scattering and 19.47 barns excluding coherent scattering (see Appendix 2). As shown in Appendix 2, for $Z = 82$ (Pb), the characteristic angle for coherent scattering of gamma-rays in the energy region relevant for the present purpose is ~ 0.1 radians; however, the half-angle subtended by the BE3825 detector at the flask axis is 0.0095 radians, and so the effect of coherent scattering ought to be included in attenuation factors. Changing the group cross-sections from 19.73 barns to 20.13 barns reduces the uncollided flux per source gamma-ray per second from $(1.60 \pm 0.16) \times 10^{-13}$ to $(1.17 \pm 0.12) \times 10^{-13} \text{ cm}^{-2} \text{ s}^{-1}$, and the resultant ^{182}Ta activity is given in Table A5.

keV	Count rate, s^{-1}	Emiss. prob.	Uncoll. flux	Flux in absence of atten.	Atten. factor	Detect. effic.	Activity TBq
^{182}Ta							
1257	0.2556 ± 0.0023	1.51%	$1.17\text{E-}13 \pm 10\%$	$6.61\text{E-}07$	$1.78\text{E-}07$	$1.57\text{E-}06 \pm 10\%$	61 ± 9
^{172}Lu							
1094	0.0367 ± 0.0026	62.50%	$5.13\text{E-}15 \pm 10\%$	$6.61\text{E-}07$	$7.76\text{E-}09$	$1.81\text{E-}06 \pm 10\%$	4.2 ± 0.7
1402	0.0062 ± 0.0008	0.72%	$1.25\text{E-}13 \pm 10\%$	$6.61\text{E-}07$	$1.90\text{E-}07$	$1.40\text{E-}06 \pm 10\%$	3.2 ± 0.6
1440	0.0053 ± 0.0007	0.60%	$1.61\text{E-}13 \pm 10\%$	$6.61\text{E-}07$	$2.43\text{E-}07$	$1.37\text{E-}06 \pm 10\%$	2.6 ± 0.5
1489	0.0123 ± 0.0008	1.15%	$2.15\text{E-}13 \pm 10\%$	$6.61\text{E-}07$	$3.25\text{E-}07$	$1.32\text{E-}06 \pm 10\%$	2.5 ± 0.4
						overall	3 ± 1

Table A5. Activities obtained from measured count rates by dividing by products of gamma-ray emission probabilities, attenuation factors and detection efficiencies. (The flux in absence of attenuation is simply $1/(4\pi R^2)$ where $R = 347$ cm, and the attenuation factor is the uncollided flux divided by the flux in absence of attenuation.)

For ^{172}Lu , none of the observed lines has an energy close to the centre of the 1000–1500-keV energy group, so activities were extracted from all four lines between 1000 and 1500 keV (the 1387-keV was rejected because of its anomalously high count rate as pointed out in [25]). Changing the group cross-section to match in turn each of the cross-sections corresponding to the four lines changes the uncollided flux from $(5.3 \pm 0.5) \times 10^{-14} \text{ cm}^{-2} \text{ s}^{-1}$ to the values listed in Table A5 (cross-sections including coherent scattering from XCOM for 1094-, 1402-, 1440- and 1489-keV gamma-rays in

lead are 22.55, 18.69, 18.39 and 18.04 barns respectively), and the resultant ^{172}Lu activities are also given in Table A5.

Appendix 2 — Mass attenuation coefficients and coherent scattering

Attenuation of gamma-rays in material between a gamma-ray source and a gamma-ray detector occurs because in passing through the material some of the gamma-rays are removed or scattered off the line between the source and the detector and so do not reach the detector. As may be found in many a text book, the three main ‘removal’ processes are photoelectric absorption, Compton scattering, and pair production. But in some circumstances there is another removal component to be considered: coherent or Rayleigh scattering, whereby a gamma-ray is scattered by an atom as a whole; and such scattering can be relevant in a ‘narrow beam’ measurement where a small angular deviation off the line joining the source to the detector means that the gamma-ray ‘misses’ the detector. A comparison of the mass attenuation coefficient for lead with and without the coherent scattering contribution is shown in Fig. A3. A convenient formula is given in [7] for the characteristic angle θ_{coh} for coherent scattering: $\theta_{\text{coh}} = 2 \arcsin(0.0133Z^{1/3}/E)$ (with E in MeV), which for atomic number $Z = 82$ and gamma-ray energies $E \cong 1$ MeV is ~ 0.1 radians. It will be seen in Appendix 1 that the half-angle subtended by an HPGe gamma-ray detector at the source of gamma-rays is much less than this value of θ_{coh} , and so in the work described therein coherent scattering ought to be included in attenuation factors.

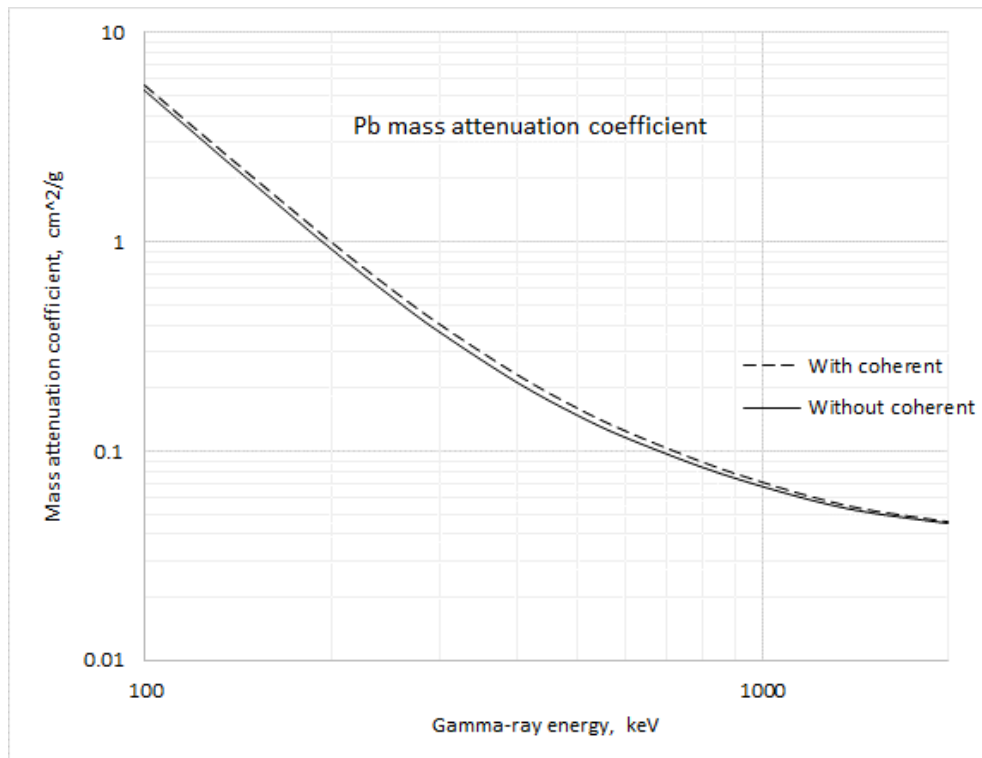


Fig. A3. Comparison of the gamma-ray mass attenuation coefficient for lead with and without coherent scattering. For gamma-ray energies such as the two ^{60}Co gamma-rays at 1173 and 1332 keV, the difference is $\sim 3\%$, not much in itself, but for attenuation along a path length of 17 cm in lead it corresponds to a difference of a factor ~ 1.45 .

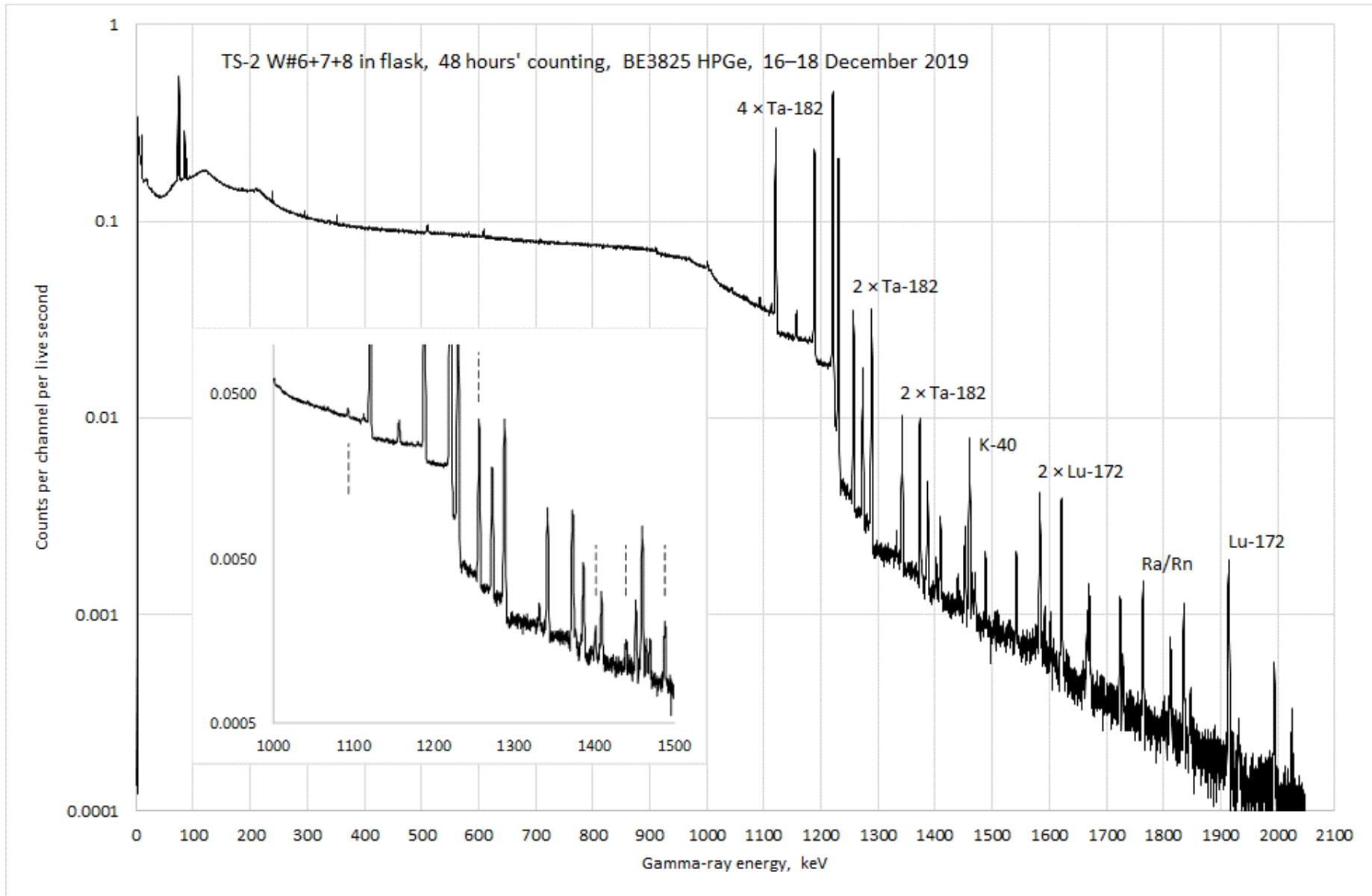


Fig. 4. Gamma-ray spectrum from TS-2 targets W#6+7+8 measured through the thick lead walls of the storage flask. The dashed lines in the inset indicate the gamma-ray lines at 1094, 1257, 1402, 1440 and 1489 keV from which activities are obtained as in Appendix 1. Some of the more prominent lines are labelled.